


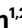

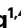




Vortex nanolaser based on a photonic disclination cavity

Received: 3 June 2023

Accepted: 19 October 2023

Published online: 27 November 2023


 Check for updates

Min-Soo Hwang ^{1,2,7}, Ha-Reem Kim ^{1,2,7}, Jungkil Kim ³, Bohm-Jung Yang ^{1,4,5},
Yuri Kivshar ⁶  & Hong-Gyu Park ¹ 

Optical vector vortex beams provide additional degrees of freedom for spatially distinguishable channels in data transmission. Although several coherent light sources carrying a topological singularity have been reported, it remains challenging to develop a general strategy for designing ultra-small, high-quality photonic nanocavities that generate and support optical vortex modes. Here we demonstrate wavelength-scale, low-threshold, vortex and anti-vortex nanolasers in a C_3 symmetric optical cavity formed by a topological disclination. Various photonic disclination cavities are designed and analysed using the similarities between tight-binding models and optical simulations. Unique resonant modes are strongly confined in these cavities, which exhibit wavelength-scale mode volumes and retain topological charges in the disclination geometries. In the experiment, the optical vortices of the lasing modes are clearly identified by measuring polarization-resolved images, Stokes parameters and self-interference patterns. Demonstration of vortex nanolasers using our facile design procedure will pave the way towards next-generation optical communication systems.

Control of the angular momentum of light has attracted a great deal of attention in photonics. The optical vector vortex is particularly useful for generating different degrees of freedom for spatially distinguishable channels in data transmission^{1–11}. Several vortex microlasers have been successfully demonstrated using microring resonators with asymmetric scatterers^{3,4}, planar spiral nanostructures⁵, micropillar chains⁶ and symmetric photonic-crystal slabs^{7,8}. Although the directional output and generation efficiency of these vortex beams are noteworthy, substantial scattering loss and large energy consumption are unavoidable when constructing ultra-small optical devices due to a lack of mechanisms for high-quality (high- Q) light confinement while maintaining the optical vortices^{3–8}. It thus remains challenging to realize low-threshold ultra-compact laser devices capable of the self-configuration of optical vortex modes and robust localization of resonant modes.

However, photonic topological insulators (PTIs) have recently been proposed as attractive tools for the robust manipulation of light^{12–18}. Studies on PTIs have been extended to topological defects in topological crystalline insulators (TCIs), such as dislocations and disclinations, which commonly disrupt the symmetric geometries of periodic structures^{19–23}. Notably, the fractional disclination charge, which belongs to the class of higher-order topological insulators (HOTIs)^{24–27}, can be trapped at the boundary of disclination defects as a topological bound state^{28–30}. Disclination defects have been experimentally demonstrated using artificial TCI metamaterials in massive domains such as microwave circuits and millimetre-scale photonic systems^{31,32}. However, the concept of disclination has not yet been applied to nanophotonics for the implementation of ultra-small light sources of quantized topological charges.

¹Department of Physics and Astronomy, Seoul National University, Seoul, Republic of Korea. ²Department of Physics, Korea University, Seoul, Republic of Korea. ³Department of Physics, Jeju National University, Jeju, Republic of Korea. ⁴Center for Theoretical Physics (CTP), Seoul National University, Seoul, Republic of Korea. ⁵Center for Correlated Electron Systems, Institute for Basic Science (IBS), Seoul, Republic of Korea. ⁶Nonlinear Physics Center, Research School of Physics, Australian National University, Canberra, Australian Capital Territory, Australia. ⁷These authors contributed equally: Min-Soo Hwang, Ha-Reem Kim.  e-mail: yuri.kivshar@anu.edu.au; hgpark@snu.ac.kr

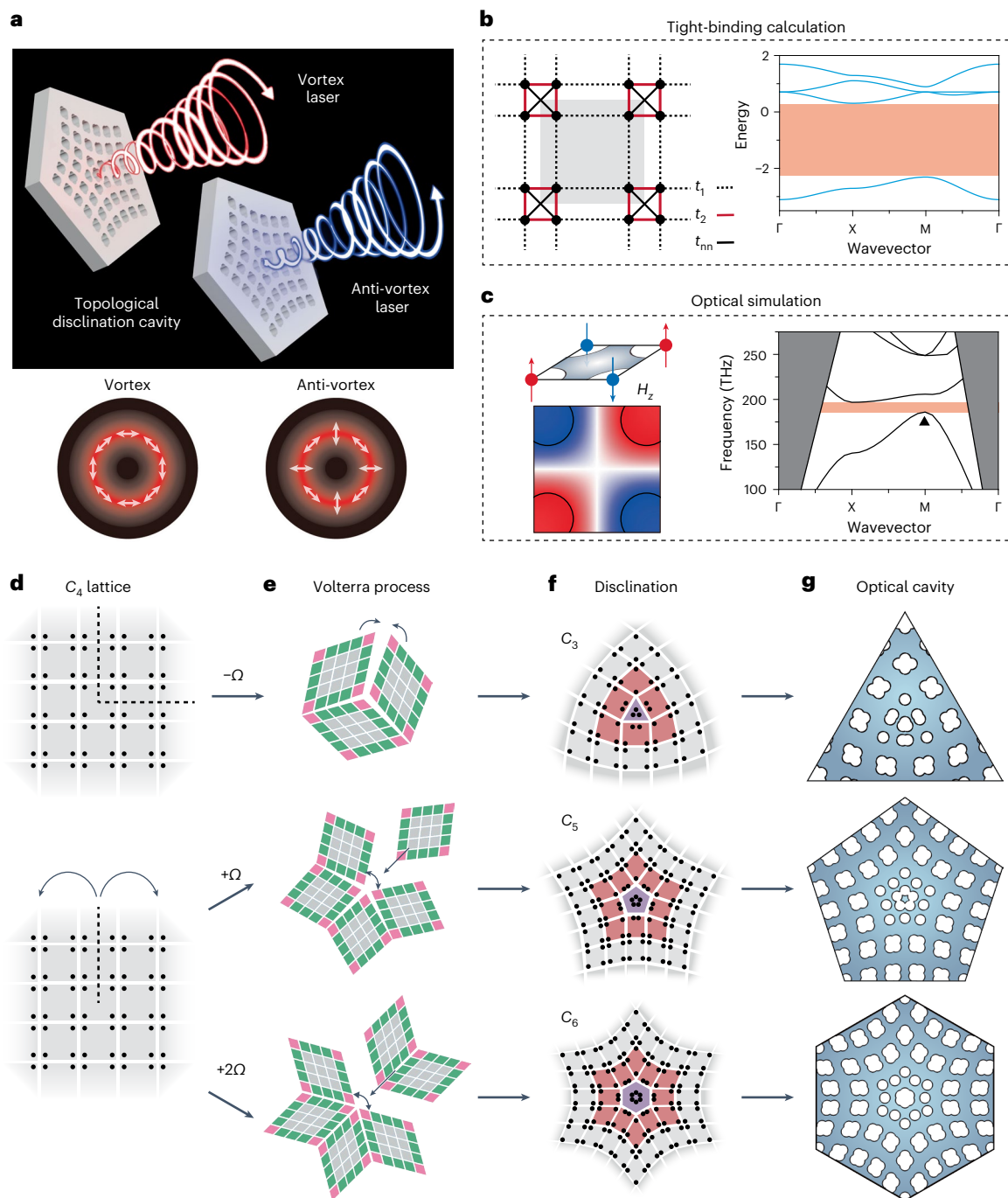


Fig. 1 | Design strategy for creating photonic disclination cavities. **a**, Top: schematic of vortex and anti-vortex disclination nanolasers. Bottom: polarization directions of optical vortex and anti-vortex modes. **b**, TB calculation of the 2D SSH lattice. Left: four discrete sites (black dots) in the C_4 symmetric lattice are connected by intra-cell coupling (t_1), inter-cell coupling (t_2) and NNN coupling (t_{nn}). The grey shaded square region indicates the unit cell. Right: calculated bandstructure with a bandgap (orange shaded area) when $t_1 = -0.2$, $t_2 = -1.0$ and $t_{nn} = t_2/\sqrt{2}$. **c**, Optical simulation of a square-lattice photonic-crystal structure. Left: the H_z -field antinodes of the quadrupole mode at the M point (black filled

triangle at the right) are confined in the four air holes at the unit cell's corner. Right: calculated photonic bandstructure with a bandgap (orange shaded area). **d–g**, Design strategy for C_3 , C_5 and C_6 symmetric photonic disclination cavities. Volterra's processes (**e**) are applied to a C_4 symmetric bulk lattice defined by HOTIs (**d**) to create C_3 (top), C_5 (middle) and C_6 (bottom) symmetric disclination geometries (**f**). Ω is the Frank angle. The three lattice colours in the unit cell in **e** indicate the regions of corner (magenta), edge (green) and bulk (grey) in the C_4 symmetric lattice. A photonic disclination cavity is formed by introducing air holes into the atomic sites of each disclination structure (**g**).

In this Article we demonstrate wavelength-scale optical vortex and anti-vortex nanolasers with topological charges of ± 1 . Using the correspondence between tight-binding (TB) models and optical simulations, various disclination geometries are converted into unprecedented optical nanocavities. Optimized optical feedback is achieved in the cores of photonic disclination cavities transformed from C_4 to C_n

symmetries ($n = 3, 5$ and 6). In the experiment, the optical vortices of all lasing modes in the C_5 symmetric photonic disclination cavity were identified by measuring polarization-resolved images, Stokes parameters and self-interference patterns. This unique design procedure for photonic disclination cavities can be utilized to develop low-threshold vortex nanolasers for next-generation optical communication systems.

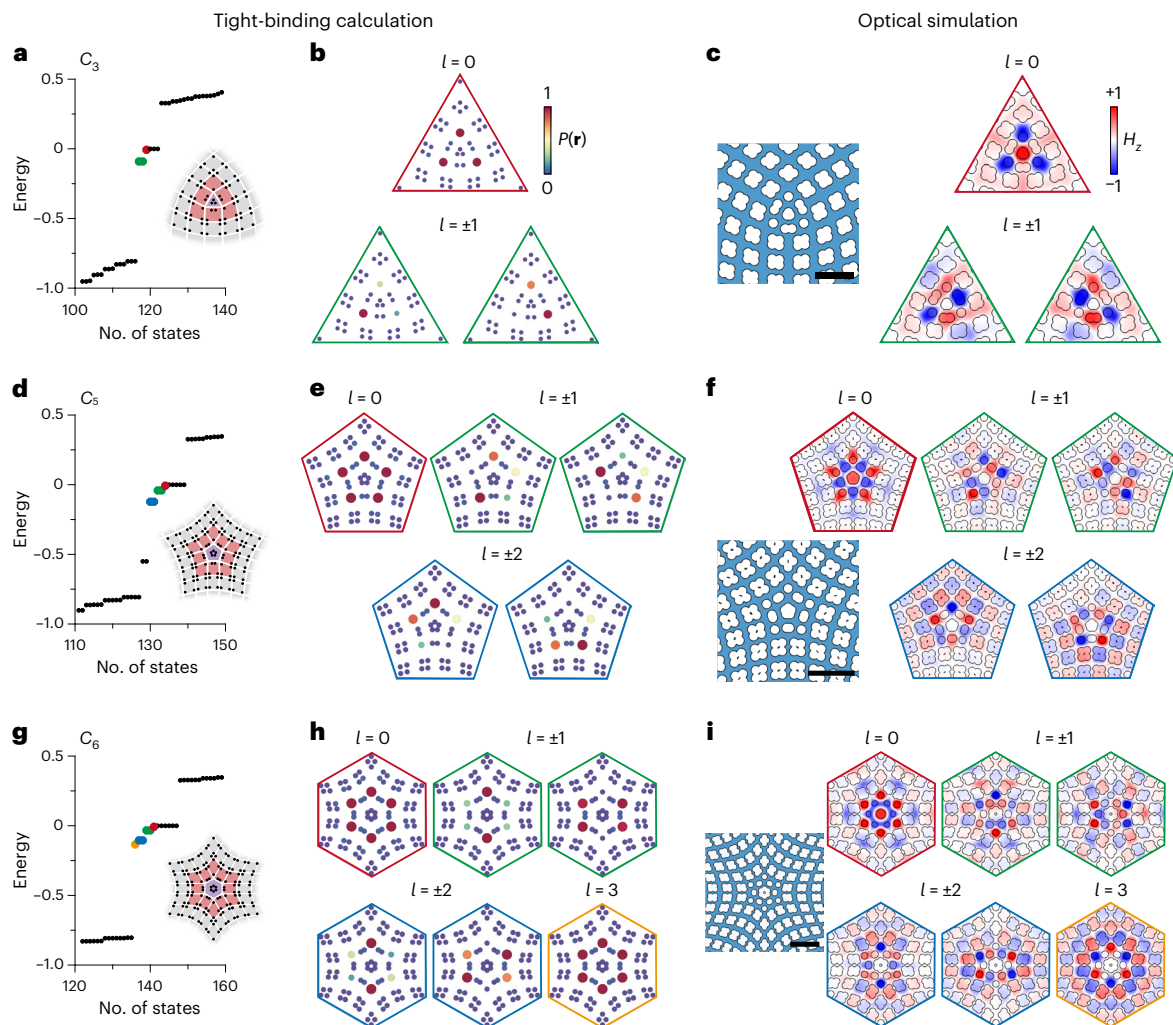


Fig. 2 | Correspondence of angular momenta in TB calculations and optical simulations. **a, b**, In-gap states of the C_3 symmetric disclination structure calculated by the TB model (**a**), and the three energy states (coloured dots in **a**) classified by probability density distributions and l (**b**). $P(r)$ in **b** indicates the probability charge density. Boundary colours in **b** are the same as the colours of the dots in **a**. **c**, Designed C_3 symmetric photonic disclination cavity (left) and calculated H_z fields of resonant modes with $l = 0$ and ± 1 (right). **d, e**, In-gap states of the C_5 symmetric disclination structure calculated by the TB model (**d**), and the five energy states (coloured dots in **d**) classified by probability density distributions and l (**e**). **f**, Designed C_5 symmetric photonic disclination

(left) and calculated H_z fields of resonant modes with $l = 0, \pm 1$ and ± 2 (right). **g, h**, In-gap states of the C_6 symmetric disclination structure calculated by the TB model (**g**), and six energy states (coloured dots in **g**) classified by probability density distributions and l (**h**). **i**, Designed C_6 symmetric photonic disclination cavity (left) and calculated H_z fields of resonant modes with $l = 0, \pm 1, \pm 2$ and 3 (right). The black dots in **a, d** and **g** indicate in-gap states confined at the structure boundaries, not in the disclination region. All resonant modes in **c, f** and **i** were calculated using 2D FEM simulation with a refractive index of 3.33 (Extended Data Fig. 3). Scale bars, $1 \mu\text{m}$ (**c, f** and **i**).

Results

Procedure for cavity design

Figure 1a shows our laser cavity, which has a disclination structure that can generate optical vortex and anti-vortex modes. Localized bound states form at the disclinations, supporting eigenstates with different angular momenta due to the C_n rotational symmetry^{20,32}. However, it is not straightforward to design high- Q photonic disclination nanocavities that not only allow for strong light confinement at the wavelength scale, but also carry eigenmodes with topological charges. To generate the desired optical vortices in a cavity, a rigorous analysis and classification of the eigenstates based on the type of disclination are required.

The TB calculation is generally used to determine the interface states of HOTIs in the two-dimensional (2D) Su–Schrieffer–Heeger (SSH) model, under the assumption of a discrete lattice structure with on-site atomic elements^{15,33,34}. For example, in a C_4 symmetric bulk lattice, a quadrumer composed of four discrete sites constructs a 2D

rectangular grid (Fig. 1b). The energy band is governed by intra-cell coupling (t_1), inter-cell coupling (t_2) and next-nearest neighbour (NNN) coupling (t_{nn}). For a comparison of the TB model with an optical simulation, we established a square-lattice photonic-crystal slab consisting of four air holes in C_4 symmetry. The fundamental transverse-electric-like (TE-like) bandstructure and field profile were calculated (Fig. 1c). The H_z -field profile at the M point presents quadrupolar antinodes confined in the four air holes at the corner (Extended Data Fig. 1).

We took advantage of the similarities between TB calculations and optical simulations—specifically, the charge density confinement in atomic sites of the TB model and the H_z -field confinement in the air holes of the optical cavity—to develop a design strategy for a photonic disclination cavity. In particular, we asked whether optical modes with angular momenta can be confined in a photonic disclination cavity, in a similar manner to fractional charges in a disclination core^{20,30,32}. Therefore, we started by solving the TB model to determine all possible

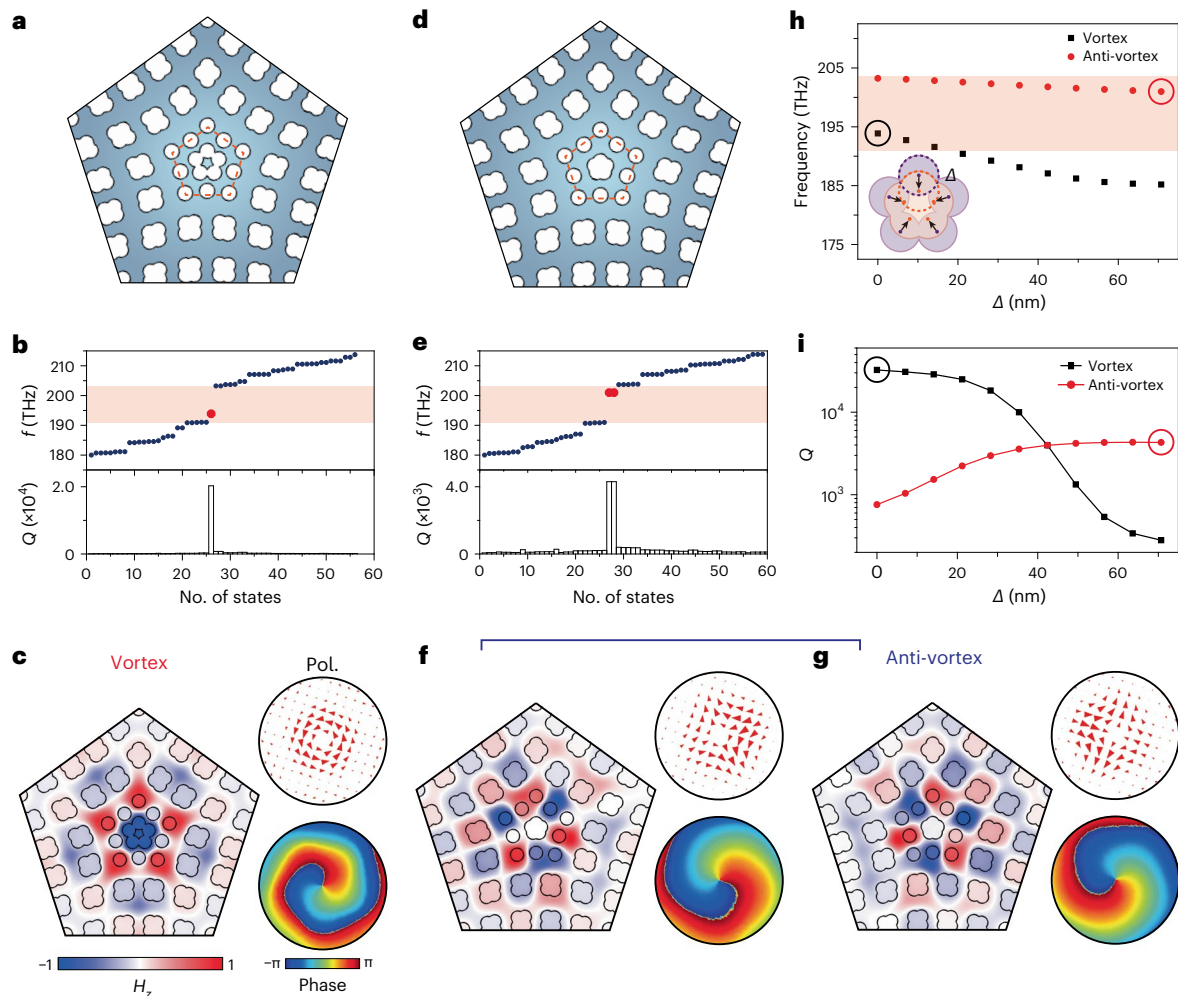


Fig. 3 | Simulated optical vortex and anti-vortex modes in C_5 symmetric photonic disclination cavities. 3D FEM simulation results for C_5 symmetric photonic disclination cavities with expanded and shrunken cores in slab structures. The C_4 symmetric bulk lattice is used to create these photonic disclination cavities with the following parameters: $a = 500$ nm, $r_0 = 0.18a$, $d_0 = 0.54a$ and $h = 275$ nm, where a , r_0 , d_0 and h are the lattice constant, radius of the air hole, centre-to-hole distance and slab thickness, respectively (Extended Data Fig. 5). The refractive index of the slab is 3.33. **a**, Photonic disclination cavity with expanded core. The air holes of the core are located $0.28a$ away from the centre. The red dashed pentagon denotes the disclination boundary. **b**, Calculated eigenmode frequencies (top) and Q factors (bottom) for the cavity of **a**. The red dot represents the resonant mode within the photonic bandgap (orange shaded area). **c**, Optical vortex mode excited in the cavity of **a**. The H_z

field (left), polarization vector field (upper right) and phase distribution (lower right) represent the vortex feature of $q = +1$. **d**, Photonic disclination cavity with shrunken core. The air-hole positions in the core differ by 71 nm from those in the expanded core. The red dashed pentagon denotes the disclination boundary. **e**, Calculated eigenmode frequencies (top) and Q factors (bottom) for the cavity in **d**. The red dots represent the doubly degenerate modes within the photonic bandgap (orange shaded area). **f, g**, Optical anti-vortex modes excited in the cavity of **d**. The H_z field (left), polarization vector field (upper right) and phase distribution (lower right) represent the anti-vortex feature of $q = -1$. **h, i**, Calculated frequencies (**h**) and Q factors (**i**) of the vortex (black dots) and anti-vortex (red dots) modes as a function of Δ , the centre-to-centre distance between air holes in the expanded and shrunken cores (inset of **h**). The black and red circles indicate the values of Δ for the cavities in **a** and **d**, respectively.

localized resonant modes and the angular momentum of each mode, and then designed a corresponding optical cavity with the same properties as the TB model.

Our design procedure was used to create C_3 , C_5 and C_6 symmetric photonic disclination cavities, starting with a C_4 symmetric bulk lattice that can be transformed into various structures through structural modification (Fig. 1d–g). By applying the Frank angle $\Omega = (\pi/2)$ to the C_4 lattice with four atomic sites (Fig. 1d), disclination geometries with C_n symmetry can be constructed via the Volterra process (Fig. 1e, f). For example, a C_3 symmetric disclination structure is created by removing one sector with $-\Omega$ from a C_4 symmetric bulk lattice and combining three identical HOTI sectors. Similarly, the C_5 and C_6 symmetric disclination structures are created by adding one sector ($+\Omega$) and two sectors ($+2\Omega$) to the C_4 lattice, respectively. Then, each atomic site is converted into an air hole to form a photonic disclination cavity (Fig. 1g).

To validate this design strategy, we compared the angular momenta of disclination structures in the TB model with those of the corresponding photonic disclination cavities from an optical simulation (Fig. 2). Here we show how disclination traps localized bound states while clarifying angular momentum characteristics in the TB calculations, and then we examine whether optical simulations of the designed photonic disclination cavities agree with the TB calculation results. To this end, the three disclination geometries depicted in Fig. 1d–g were investigated using TB calculations. Detailed structural parameters and simulation conditions for each symmetry are shown in Extended Data Fig. 2. The calculation results show that localized bound states of C_n symmetric disclination structures appear in the bandgap and are classified by probability density distributions with angular momenta l associated to the relative phase between the interior corners (Fig. 2, left column).

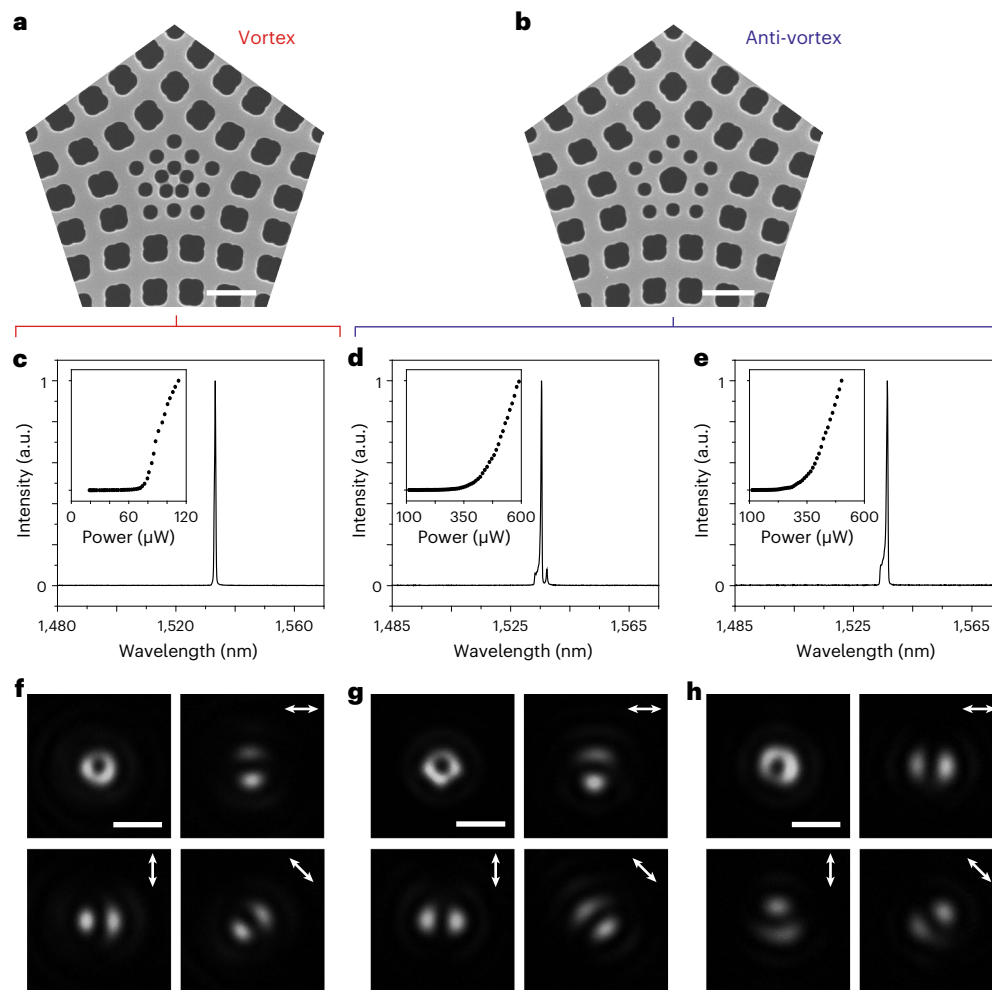


Fig. 4 | Experimental vortex and anti-vortex nanolasers. **a, b**, Scanning electron microscopy images of fabricated photonic disclination cavities with the expanded core (**a**; vortex) and shrunken core (**b**; anti-vortex). Scale bars, 500 nm. **c–e**, Measured above-threshold PL spectra and L–L curves (insets) from the cavities of **a** (**c**) and **b** (**d** and **e**). The peak wavelengths and lasing thresholds are 1,533.3 nm and 80 μ W (**c**), 1,535.4 nm and 412 μ W (**d**) and 1,536.4 nm and 346 μ W

(**e**), respectively. The spectra in **d** and **e** are from doubly degenerate modes. **f–h**, Measured polarization-resolved lasing images from the cavities of **a** (**f**) and **b** (**g** and **h**). The mode profiles were captured after placing a linear polarizer in front of the IR camera (Methods). White arrows indicate the directions of the linear polarizer: 0°, 45°, 90°. Images captured without a linear polarizer are shown in the top left panels. Scale bars, 3 μ m.

In the case of the C_3 symmetric disclination, one non-degenerate energy state and two degenerate states are observed at a near-zero energy level (Fig. 2a). These three energy states are classified by index l , and are related to the point group symmetry between the three interior corners, as calculated in the probability density distributions of eigenvectors (Fig. 2b). Similarly, five and six eigenstates are observed at near-zero energy levels for the C_5 and C_6 symmetric disclinations, respectively (Fig. 2d,e,g,h). All these states in the probability density distributions with l are localized to the interior corner sites. Taken together, the C_n point group symmetry is satisfied by the localization of probability charge density at the C_n symmetric interior corners ($n = 3, 5$ and 6), and the energy states of l exhibit the relation $\psi(r, \varphi + \frac{2\pi}{n}) = \psi(r, \varphi) e^{i2\pi l/n}$, where ψ is the eigenvector or the H_z -field profile in the polar coordinate.

Next, we created photonic disclination cavities using the above TB calculations to derive eigenmodes with l (Fig. 2, right column). As described in the design strategy in Fig. 1g, the atomic sites are replaced by air holes. The air-hole positions and spacings are determined by the coupling strengths t_1 , t_2 and t_{nn} in the TB model. We then performed 2D finite-element method (FEM) simulations to calculate the H_z fields and angular momenta of the resonant modes excited in the

C_3 , C_5 and C_6 symmetric photonic disclination cavities (Methods and Extended Data Fig. 3). The FEM simulations reveal resonant modes confined to the disclination region that are almost identical to the TB results (Fig. 2c,f,i). This one-to-one correspondence between the topological and photonic (H_z) in-gap states, with the same angular momenta, originates from the similarities between TB and optical simulations. We note that no resonant mode is localized in the core of a photonic disclination cavity made using a trivial unit cell (Extended Data Fig. 4).

Vector vortex analysis and optical simulations

The modes with $l = 0$ and $l = \pm 2$ in the C_5 symmetric photonic disclination cavity are of particular interest because they have central singularities in the electric fields. To excite these modes in a 3D cavity, the C_5 symmetric photonic disclination cavity of Fig. 2f was formed in a photonic-crystal slab structure (Fig. 3). We calculated their topological charges, defined as $q = 1/2\pi \oint_C d\varphi \partial_\varphi \arg E(r, \varphi)$ (ref. 35), to examine the optical vortices. First, when considering the TE modes, the electric field of the C_5 disclination mode with $l = 0$ is given by

$$\mathbf{E}_{l=0} = u_0(r) \{ e^{i\varphi} \hat{\mathbf{e}}_R - e^{-i\varphi} \hat{\mathbf{e}}_L \} \quad (1)$$

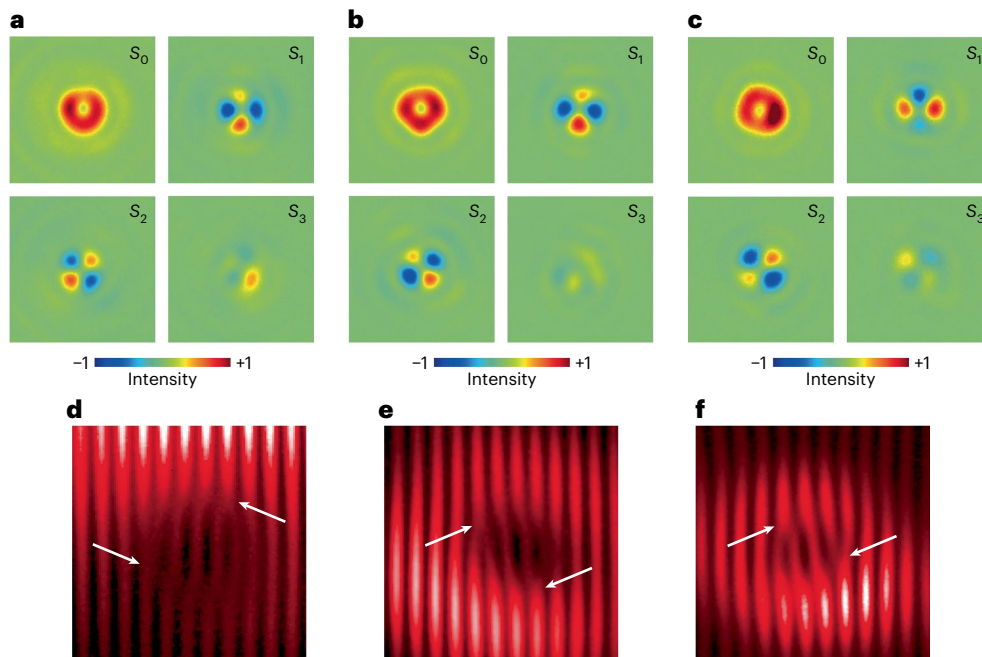


Fig. 5 | Evidence for vortex and anti-vortex modes. **a–c**, Stokes parameters of vortex and anti-vortex modes obtained from Fig. 4f (**a**), 4g (**b**) and 4h (**c**). Complete sets of measured polarization-resolved mode images are shown in

Extended Data Fig. 8. **d–f**, Measured self-interference patterns of the vortex (**d**) and anti-vortex lasing modes (**e** and **f**), corresponding to **a**, **b** and **c**, respectively. The fork fringes are marked with arrows.

where $u_0(r)$ is a radial part of the electric field, and \hat{e}_R and \hat{e}_L are the right- and left-circular polarization bases, respectively (Supplementary Note 1). q is then calculated as $+1$, which is the vortex mode, also known as the azimuthal polarization state^{36,37}. In addition, the electric-field profiles of anti-vortex modes are produced by disclination modes with $l = \pm 2$ as follows:

$$\mathbf{E}_+ = u_+(r)\{e^{i\varphi}\hat{e}_L - e^{-i\varphi}\hat{e}_R\} \quad (2)$$

$$\mathbf{E}_- = u_-(r)\{e^{i\varphi}\hat{e}_L + e^{-i\varphi}\hat{e}_R\} \quad (3)$$

which denote even and odd hybrid polarized states with radial electric-field components of $u_+(r)$ and $u_-(r)$, respectively^{36,37}. These are the anti-vortex modes, with q values calculated as -1 . As a result of the superposition of $\pm(|l| - 1)$ (Supplementary Note 1), polarization vortices are formed^{7,37–39}.

As in the 2D case, we designed a 3D photonic disclination cavity by merging four, two and five air holes in the bulk, disclination boundary and core, respectively (Fig. 3a,d and Extended Data Fig. 5). The periodic air holes in the bulk open a photonic bandgap into which the defect resonant modes localized in the disclination region are introduced (Fig. 3b,e). In addition, the air holes at the disclination boundary are modified to excite different types of resonant mode with higher Q factors (Fig. 3a,d, red dashed pentagons). Without this modification in the disclination boundary, only the vortex mode is excited, even if the shape of the core changes (Extended Data Fig. 6).

We then performed systematic 3D FEM simulations in the photonic disclination slab cavities with expanded and shrunken cores to calculate the frequencies and Q factors of the resonant modes. The disclination structures are made of an InGaAsP slab with a thickness of 275 nm and lattice constant of 500 nm (Extended Data Fig. 5). In the photonic disclination cavity with expanded core (Fig. 3a), a single mode with a Q factor of 2.0×10^4 at 193.9 THz was calculated as an in-gap resonant state (Fig. 3b). The calculated mode volume was $0.58 (\lambda/n)^3$, where λ and n are the resonant wavelength and refractive index of the

slab, respectively. We also obtained near-field and far-field profiles for this mode, including the H_z field, polarization vector field and phase distribution. The H_z field was strongly confined in the five interior air holes and disclination core (Fig. 3c), which corresponds to the eigenstate with $l = 0$ in Fig. 2f. The polarization vector distribution exhibits an azimuthal polarization state with a singularity at the centre. Also, the phase of $(E_x + iE_y)$, the winding number of the polarization, represents a counterclockwise closed loop around the singularity³⁵, which indicates a vortex mode, $q = +1$.

We also modified a core design by shrinking the core to excite a different type of mode (Fig. 3d). The structural parameters are the same as in Fig. 3a, except for the disclination core. Doubly degenerated modes were then excited in this shrunken-core photonic disclination cavity, showing Q factors of 4.3×10^3 at 201.0 THz (Fig. 3e). Their mode volumes were calculated to be $0.61 (\lambda/n)^3$, indicating light confinement at the wavelength scale. In addition, the distinguishable features from those in Fig. 3c are displayed in the calculated field profiles (Fig. 3f,g). Strong confinements in the H_z profiles are observed only at the disclination boundaries, not at the cores, which correspond to the eigenstates with $l = \pm 2$ in Fig. 2f. In Fig. 3f,g, the polarization vector distributions are referred to as odd and even hybrid polarized states, respectively. Also, because the phase of $(E_x + iE_y)$ is given by a clockwise closed loop around the central singularity, both modes exhibit the anti-vortex feature, $q = -1$.

Furthermore, the FEM simulation showed the mode transition from optical vortex to anti-vortex mode by shrinking the core. We calculated the frequencies (Fig. 3h) and Q factors (Fig. 3i) of the resonant modes as a function of Δ , the centre-to-centre distance between air holes in the core. The frequency of the vortex mode decreased as Δ increased from the expanded core, eventually moving out of the bandgap with a substantial decrease in Q . In contrast, the anti-vortex mode moved from the higher-frequency region to the bandgap with a reasonably high Q factor. This local deformation of the disclination core can increase the Q factor of a specific mode, allowing mode transition with desired polarization distributions and topological charges.

Measurements of vortex/anti-vortex nanolasers

For the experimental demonstration of vortex and anti-vortex nanolasers, we fabricated two types of photonic disclination cavity in a 287-nm-thick InGaAsP slab with three quantum wells (Methods). As designed using the FEM simulation in Fig. 3, the disclination core consisting of five air holes moved radially to form expanded or shrunken ones (Fig. 4a,b). The photonic disclination cavities were optically pumped at room temperature with a 980-nm laser diode at a repetition rate of 1 MHz and a 2% duty cycle (Methods). We then measured photoluminescence (PL) spectra and light-in-light-out (L-L) curves (Fig. 4c–e). Each cavity exhibited clear lasing features, including a sharp single-mode peak and a super-linear growth above the threshold. The divergence angle of the emitted beams was measured to be 34.5°. The slightly different wavelengths and threshold values between degenerate modes (Fig. 4d,e) originated from fabrication imperfections.

We examined the polarization-resolved mode images (Fig. 4f–h), which show the following unique properties. First, without a polarizer, all lasing modes displayed doughnut-shaped intensity profiles (top left). The intensity node in the centre is one of the distinguishable features of vortex/anti-vortex modes. In addition, the polarization-resolved mode images in each mode are fully distinguishable. For example, images with an intensity minimum along the polarizer axis were observed in the photonic disclination cavity with an expanded core, indicating the azimuthal polarization state (Fig. 4f). On the other hand, in the cavity with shrunken core, the two degenerate modes exhibited more complicated images that are completely opposite to each other (Fig. 4g,h). These images correspond to the odd and even hybrid polarization states. The measured images agree well with the simulated ones (Extended Data Fig. 7), demonstrating the effectiveness of our design strategy.

Next, to quantitatively assess the purity of the vectorial states in the lasing modes, we analysed spatially resolved Stokes parameters⁴⁰. To this end, we measured complete sets of polarization-resolved mode images from the vortex and anti-vortex lasers, including 0°, ±45° and 90° linearly polarized images and right/left circularly polarized images (Extended Data Fig. 8). Figure 5a–c shows the Stokes parameters (S_0 , S_1 , S_2 and S_3) obtained from these polarization-resolved images (Methods). In all three cases, S_1 and S_2 consist of four intensity lobes that are rotated 45° from each other, whereas S_3 has a weak intensity profile, indicating that the vector beam is of high quality⁴¹. Specifically, the Stokes parameters in Fig. 5a display the azimuthal polarization distribution of the vortex beam. The colour distributions in S_2 in Fig. 5b and S_1 in Fig. 5c are opposite to those in Fig. 5a, demonstrating the anti-vortex feature. We observe a non-perfectly zero S_3 mainly due to the small laser size and fabrication imperfections (Supplementary Fig. 1).

Furthermore, self-interference patterns were measured in the vortex and anti-vortex lasing modes^{3,7} (Methods and Supplementary Fig. 2). The measured patterns using an off-centre self-interferometry set-up show that all modes have a pair of correct and inverted fork fringes⁷ (Fig. 5d–f). We observe that the order of the fork fringes differs between the two disclination cavities. These interference results, as well as the polarization-resolved mode images and Stokes parameters, show that the expanded core cavity has $q = +1$ (vortex), whereas the shrunken-core cavity has $q = -1$ (anti-vortex). Therefore, we have successfully demonstrated vortex and anti-vortex nanolasers that were strongly confined in the photonic disclination cavities, as designed in the TB models and FEM simulations of Figs. 2 and 3. We note that the mode transition between these vortex and anti-vortex lasing modes can occur simply by changing the core, whereas there is no transition in a photonic disclination cavity without modifying the disclination boundary (Extended Data Fig. 9).

Discussion

We have introduced and experimentally realized novel nanolasers generating optical vortices from wavelength-scale photonic disclination

cavities with C_n symmetry. The facile design approach based on the exceptional correlation between TB models and optical simulations has been developed to transform various topological disclinations into unprecedented optical nanocavities. The vortex and anti-vortex modes with $q = \pm 1$ were obtained in a C_3 symmetric photonic disclination cavity (Supplementary Note 2). Our strategy was also used to design resonant modes with $|q| = 2$ or a radial polarization state in C_6 symmetric hole-type and C_5 symmetric rod-type photonic disclination cavities, respectively (Extended Data Fig. 10). Furthermore, our disclination nanolaser outperforms other types of vortex laser in terms of lasing threshold and cavity size (Supplementary Table 1).

This demonstration will be useful for the development of the ultimate laser sources with superior optical properties, such as small footprint, low threshold and self-configuration of vortex modes. Through vector mode multiplexing, various vector vortex beams can be generated that are suitable for increasing the capacity of optical communications^{39,42,43}. Multiple data streams can be transmitted simultaneously by encoding information into different vector beams. Furthermore, vortex nanolasers can have a fast modulation speed due to their small mode volume, and thus will be a promising technology for providing a new platform for high-bandwidth optical communication.

Online content

Any methods, additional references, Nature Portfolio reporting summaries, source data, extended data, supplementary information, acknowledgements, peer review information; details of author contributions and competing interests; and statements of data and code availability are available at <https://doi.org/10.1038/s41566-023-01338-2>.

References

- Allen, L., Beijersbergen, M. W., Spreeuw, R. J. C. & Woerdman, J. P. Orbital angular momentum of light and the transformation of Laguerre-Gaussian laser modes. *Phys. Rev. A* **45**, 8185–8189 (1992).
- Ni, J. et al. Multidimensional phase singularities in nanophotonics. *Science* **374**, eabj0039 (2021).
- Miao, P. et al. Orbital angular momentum microlaser. *Science* **353**, 464–467 (2016).
- Zhang, Z. et al. Tunable topological charge vortex microlaser. *Science* **368**, 760–763 (2020).
- Sun, W. et al. Lead halide perovskite vortex microlasers. *Nat. Commun.* **11**, 4862 (2020).
- Carlou Zambon, N. et al. Optically controlling the emission chirality of microlasers. *Nat. Photon.* **13**, 283–288 (2019).
- Huang, C. et al. Ultrafast control of vortex microlasers. *Science* **367**, 1018–1021 (2020).
- Mohamed, S. et al. Controlling topology and polarization state of lasing photonic bound states in continuum. *Laser Photon. Rev.* **16**, 2100574 (2022).
- Sroor, H. et al. High-purity orbital angular momentum states from a visible metasurface laser. *Nat. Photon.* **14**, 498–503 (2020).
- Zhang, X., Liu, Y., Han, J., Kivshar, Y. & Song, Q. Chiral emission from resonant metasurfaces. *Science* **377**, 1215–1218 (2022).
- Zhang, Z. et al. Spin-orbit microlaser emitting in a four-dimensional Hilbert space. *Nature* **612**, 246–251 (2022).
- Bahari, B. et al. Nonreciprocal lasing in topological cavities of arbitrary geometries. *Science* **358**, 636–640 (2017).
- Bandres, M. A. et al. Topological insulator laser: experiments. *Science* **359**, eaar4005 (2018).
- Ota, Y. et al. Topological photonic crystal nanocavity laser. *Commun. Phys.* **1**, 86 (2018).
- Kim, H.-R. et al. Multipolar lasing modes from topological corner states. *Nat. Commun.* **11**, 5758 (2020).
- Yang, Z.-Q., Shao, Z.-K., Chen, H.-Z., Mao, X.-R. & Ma, R.-M. Spin-momentum-locked edge mode for topological vortex lasing. *Phys. Rev. Lett.* **125**, 013903 (2020).

17. Bahari, B., Choi, J.-H., Liu, Y. G. N. & Khajavikhan, M. Majorana bound state cavities. *Phys. Rev. B* **104**, 235423 (2021).
18. Yang, L. et al. Topological-cavity surface-emitting laser. *Nat. Photon.* **16**, 279–283 (2022).
19. Wang, Q., Xue, H., Zhang, B. & Chong, Y. D. Observation of protected photonic edge states induced by real-space topological lattice defects. *Phys. Rev. Lett.* **124**, 243602 (2020).
20. Wang, Q. et al. Vortex states in an acoustic Weyl crystal with a topological lattice defect. *Nat. Commun.* **12**, 3654 (2021).
21. Xie, B. et al. Higher-order band topology. *Nat. Rev. Phys.* **3**, 520–532 (2021).
22. Xie, B. Y., You, O. & Zhang, S. Photonic topological pump between chiral disclination states. *Phys. Rev. A* **106**, L021502 (2022).
23. Lustig, E. et al. Photonic topological insulator induced by a dislocation in three dimensions. *Nature* **609**, 931–935 (2022).
24. Benalcazar, W. A., Andrei Bernevig, B. & Hughes, T. L. Quantized electric multipole insulators. *Science* **357**, 61–66 (2017).
25. Mittal, S. et al. Photonic quadrupole topological phases. *Nat. Photon.* **13**, 692–696 (2019).
26. Noh, J. et al. Topological protection of photonic mid-gap defect modes. *Nat. Photon.* **12**, 408–415 (2018).
27. Kirsch, M. S. et al. Nonlinear second-order photonic topological insulators. *Nat. Phys.* **17**, 995–1000 (2021).
28. Peterson, C. W., Li, T., Benalcazar, W. A., Hughes, T. L. & Bahl, G. A fractional corner anomaly reveals higher-order topology. *Science* **368**, 1114–1118 (2020).
29. Benalcazar, W. A., Li, T. & Hughes, T. L. Quantization of fractional corner charge in C_n -symmetric higher-order topological crystalline insulators. *Phys. Rev. B* **99**, 245151 (2019).
30. Li, T., Zhu, P., Benalcazar, W. A. & Hughes, T. L. Fractional disclination charge in two-dimensional C_n -symmetric topological crystalline insulators. *Phys. Rev. B* **101**, 115115 (2020).
31. Peterson, C. W., Li, T., Jiang, W., Hughes, T. L. & Bahl, G. Trapped fractional charges at bulk defects in topological insulators. *Nature* **589**, 376–380 (2021).
32. Liu, Y. et al. Bulk-disclination correspondence in topological crystalline insulators. *Nature* **589**, 381–385 (2021).
33. Xie, B.-Y. et al. Visualization of higher-order topological insulating phases in two-dimensional dielectric photonic crystals. *Phys. Rev. Lett.* **122**, 233903 (2019).
34. He, L., Addison, Z., Mele, E. J. & Zhen, B. Quadrupole topological photonic crystals. *Nat. Commun.* **11**, 3119 (2020).
35. Berry, M. V. Optical vortices evolving from helicoidal integer and fractional phase steps. *J. Opt. A Pure Appl. Opt.* **6**, 259 (2004).
36. Galvez, E. J., Khadka, S., Schubert, W. H. & Nomoto, S. Poincaré-beam patterns produced by nonseparable superpositions of Laguerre-Gauss and polarization modes of light. *Appl. Opt.* **51**, 2925–2934 (2012).
37. Rosales-Guzmán, C., Ndagano, B. & Forbes, A. A review of complex vector light fields and their applications. *J. Opt.* **20**, 123001 (2018).
38. Doleman, H. M., Monticone, F., Hollander, W. D., Alù, A. & Koenderink, A. F. Experimental observation of a polarization vortex at an optical bound state in the continuum. *Nat. Photon.* **12**, 397–401 (2018).
39. Shen, Y. et al. Optical vortices 30 years on: OAM manipulation from topological charge to multiple singularities. *Light Sci. Appl.* **8**, 90 (2019).
40. Selyem, A., Rosales-Guzmán, C., Croke, S., Forbes, A. & Franke-Arnold, S. Basis-independent tomography and nonseparability witnesses of pure complex vectorial light fields by Stokes projections. *Phys. Rev. A* **100**, 063842 (2019).
41. Liu, Y. et al. Realization of polarization evolution on higher-order Poincaré sphere with metasurface. *Appl. Phys. Lett.* **104**, 191110 (2014).
42. Wang, J. et al. Orbital angular momentum and beyond in free-space optical communications. *Nanophotonics* **11**, 645–680 (2022).
43. Naidoo, D. et al. Controlled generation of higher-order Poincaré sphere beams from a laser. *Nat. Photon.* **10**, 327–332 (2016).

Publisher's note Springer Nature remains neutral with regard to jurisdictional claims in published maps and institutional affiliations.

Open Access This article is licensed under a Creative Commons Attribution 4.0 International License, which permits use, sharing, adaptation, distribution and reproduction in any medium or format, as long as you give appropriate credit to the original author(s) and the source, provide a link to the Creative Commons license, and indicate if changes were made. The images or other third party material in this article are included in the article's Creative Commons license, unless indicated otherwise in a credit line to the material. If material is not included in the article's Creative Commons license and your intended use is not permitted by statutory regulation or exceeds the permitted use, you will need to obtain permission directly from the copyright holder. To view a copy of this license, visit <http://creativecommons.org/licenses/by/4.0/>.

© The Author(s) 2023

Methods

TB calculations

The TB model can be used to calculate the topological energy states and angular momenta when the structural lattice undergoes complex transformations such as disclination³⁰. We performed TB calculations (Python) for the 2D SSH model including NNN hopping. The C_4 symmetric SSH lattice with four discrete sites (Fig. 1b) was connected by weak intra-cell coupling ($t_1 = -0.2$) and strong inter-cell coupling ($t_2 = -1.0$), with additionally incorporated NNN coupling ($t_{nn} = t_2/\sqrt{2}$). The lattice constant was set as 1. The C_n symmetric disclination geometries (Fig. 1f) consisted of a bulk lattice (grey) and a disclination region (magenta and purple) with 13 unit cells per side. The bulk lattice obeys the coupling of the SSH lattice, and the modification of coupling occurs only in the disclination region (Extended Data Fig. 2). Volterra's process in our TB model does not violate the C_4 symmetry of the lattice, and disclination boundary effects only alter the energy levels of the disclination states. In addition, the spatial probability density $P(\mathbf{r})$ is given by $P(\mathbf{r}) = |\psi(\mathbf{r})|^2$, where $\psi(\mathbf{r})$ is an eigenvector (Fig. 2). The angular momentum l is represented by the phase shift at neighbouring interior corners of the eigenvector.

FEM simulations

The 2D (Fig. 2) and 3D (Fig. 3) FEM simulations (COMSOL Multiphysics) were performed to calculate optical resonant modes and bandstructures. Floquet periodic boundaries and perfectly matched layers were used in the lateral and out-of-plane directions, respectively. The geometries of the TB model were used to derive the structural parameters of the photonic disclination cavities (Extended Data Figs. 3 and 5). The refractive index of the dielectric material was 3.33. The angular momentum l was determined by the resonant frequency and far-field profile of each eigenmode. In addition, far-field images of the polarization vector fields and phase distributions were calculated at 1.5 μm above the slab surface.

Device fabrication

The samples were fabricated using a 287-nm-thick InGaAsP/1- μm -thick InP/100-nm-thick InGaAs/InP substrate wafer. The InGaAsP layer included three quantum wells in the middle, whose central emission wavelength was $\sim 1.55 \mu\text{m}$. The InP and InGaAs layers served as sacrificial and etch stop layers, respectively. The designed patterns using the COMSOL simulation were directly converted to CAD to define air holes in a photonic disclination cavity, and electron-beam lithography was performed at 30 keV on a poly(methyl methacrylate) (PMMA) layer coated on the wafer. Chemically assisted ion-beam etching was performed to drill air holes into the InGaAsP layer while using the PMMA layer as an etch mask. Finally, the sacrificial InP layer was selectively wet etched using a diluted HCl:H₂O (4:1) solution at room temperature, and the remaining PMMA layer on top of the slab was removed by O₂ plasma.

Optical measurements

A 980-nm pulsed laser diode (2.0% duty cycle, 1-MHz period) with a spot size of $\sim 3 \mu\text{m}$ was used to optically pump the fabricated samples at room temperature. The light emitted from the photonic disclination cavities was collected by a $\times 100$ objective lens with a numerical aperture of 0.85 (LCPLN100XIR, Olympus) and focused onto a spectrometer equipped with an infrared array detector (SP 2300i and PyLoN, Princeton Instruments) or an InGaAs infrared camera (PA1280F70NCL, OZRAY, 1,280 \times 1,024 pixels). The resolution of the spectrometer was $\sim 0.5 \text{ nm}$. The measured L-L curves were plotted as a function of the peak pump power (Fig. 4c–e insets and Extended Data Fig. 9b). The polarization-resolved mode images were captured after placing a half-wave plate and polarizing beamsplitter (for linearly polarized images) or a quarter-wave plate, half-wave plate and polarizing beamsplitter (for circularly polarized images) in front of the infrared camera (Fig. 4f–h and Extended Data Figs. 8 and 9c).

Stokes parameters

We obtained spatially resolved Stokes parameters by measuring the intensity of the laser beam in six polarizations: horizontal (I_H), vertical (I_V), diagonal (I_D), antidiagonal (I_A), right circular (I_R) and left circular (I_L). The Stokes parameters were as follows: $S_0 = I_H + I_V$, $S_1 = I_H - I_V$, $S_2 = I_D - I_A$ and $S_3 = I_R - I_L$. All parameters were normalized by the total intensity, S_0 .

Off-centre self-interference measurements

The optical vortex of the lasing mode was measured using the off-centre self-interferometry set-up. In this set-up, the lasing mode was split into two paths by a beamsplitter and reconverged in image space, forming the self-interference pattern. To clearly observe this interference pattern, the central singularities of the vortex and anti-vortex lasing modes were slightly off-centre and magnified by a pair of the concave and convex lenses in front of the infrared camera (Supplementary Fig. 2). The self-interference pattern obtained with such an off-centred overlap revealed a pair of fork fringes.

Data availability

All the data supporting the findings of this study are available within this Article and its Supplementary Information. Any additional information can be obtained from the corresponding authors on reasonable request. Source data are provided with this paper.

Code availability

The codes used in this work are available from the corresponding authors upon reasonable request.

Acknowledgements

We thank D. Leykam for helpful discussions. This work was supported by a National Research Foundation of Korea (NRF) grant funded by the Korean Government (MSIT) (nos. 2021R1A2C3006781, 2022R111A1A01073189 and 2022R111A1A01072807). H.-G.P. was supported by the Institute of Applied Physics, Seoul National University. Y.K. was supported by the Australian Research Council (grant nos. DP200101168 and DP210101292) and the International Technology Center Indo-Pacific (ITC IPAC) via Army Research Office (contract FA520923C0023). B.-J.Y. was supported by the Institute for Basic Science in Korea (grant no. IBS-R009-D1), the Samsung Science and Technology Foundation (project no. SSTF-BA2002-06) and NRF grants (nos. 2021R1A2C4002773 and NRF-2021R1A5A1032996).

Author contributions

M.-S.H., Y.K. and H.-G.P. conceived the idea. M.-S.H. designed the cavities and conducted the simulations. M.-S.H. and H.-R.K. fabricated the samples and performed the optical measurements. M.-S.H., H.-R.K., J.K., B.-J.Y., Y.K. and H.-G.P. analysed the experimental and theoretical data. All authors contributed to writing and editing the manuscript.

Competing interests

The authors declare no competing interests.

Additional information

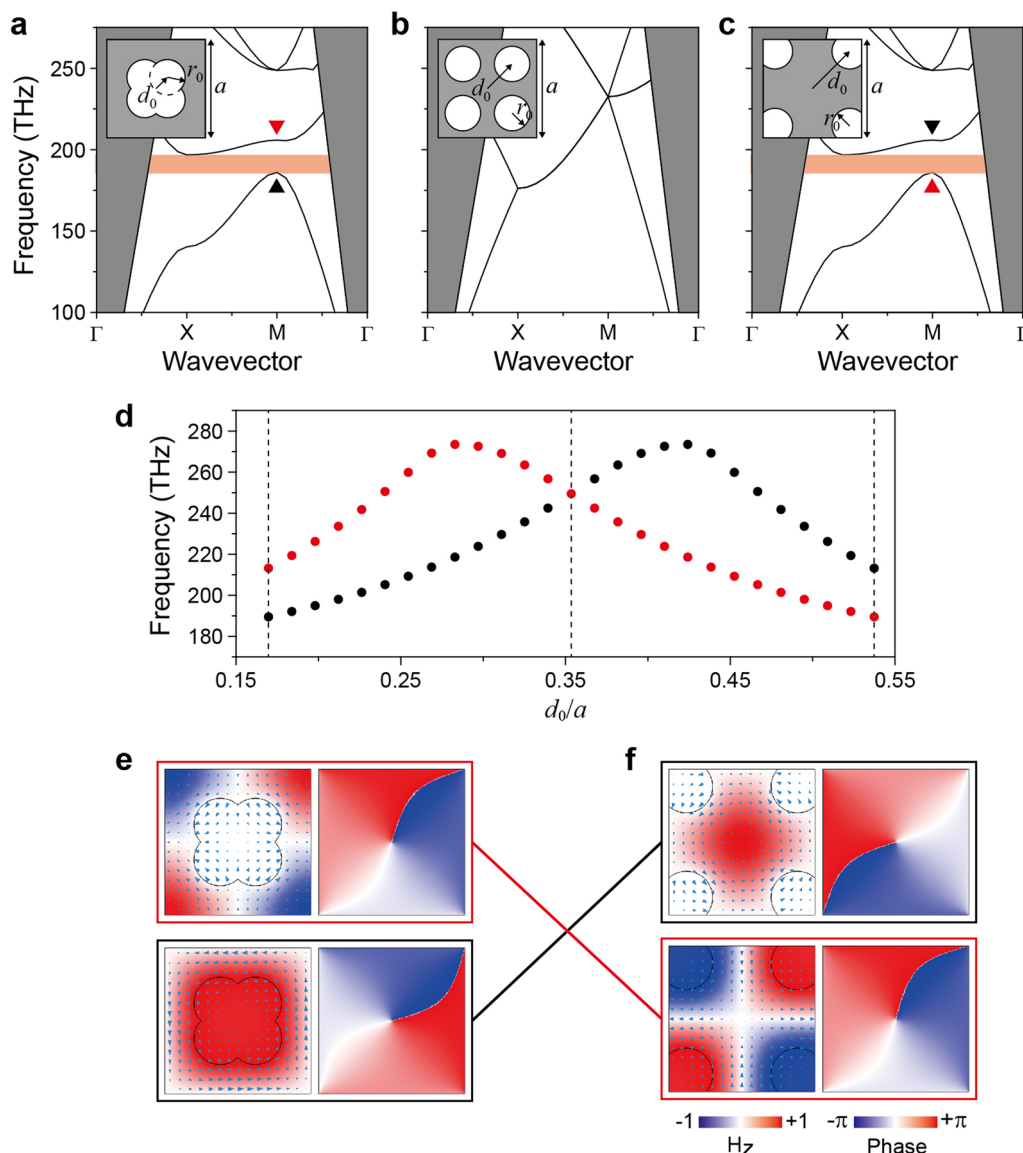
Extended data is available for this paper at <https://doi.org/10.1038/s41566-023-01338-2>.

Supplementary information The online version contains supplementary material available at <https://doi.org/10.1038/s41566-023-01338-2>.

Correspondence and requests for materials should be addressed to Yuri Kivshar or Hong-Gyu Park.

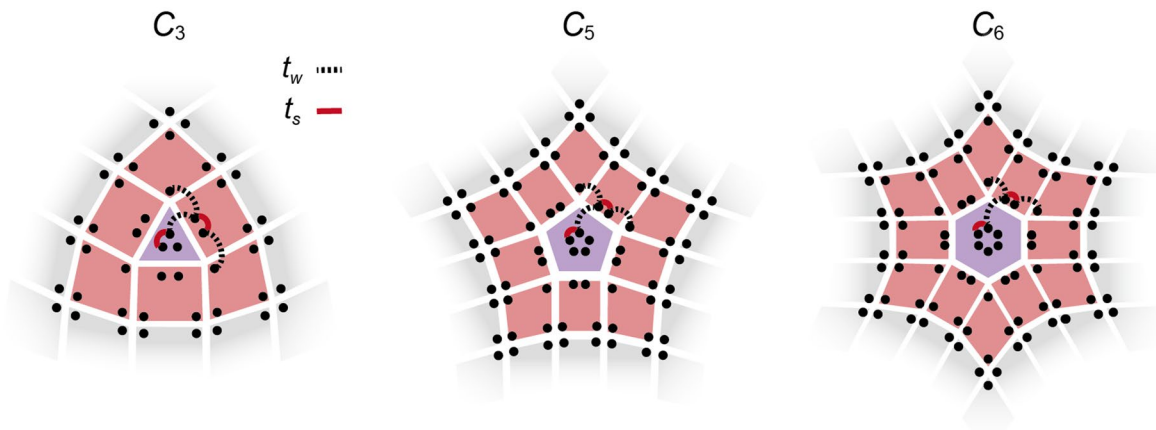
Peer review information *Nature Photonics* thanks Andrew Forbes and the other, anonymous, reviewer(s) for their contribution to the peer review of this work.

Reprints and permissions information is available at www.nature.com/reprints.



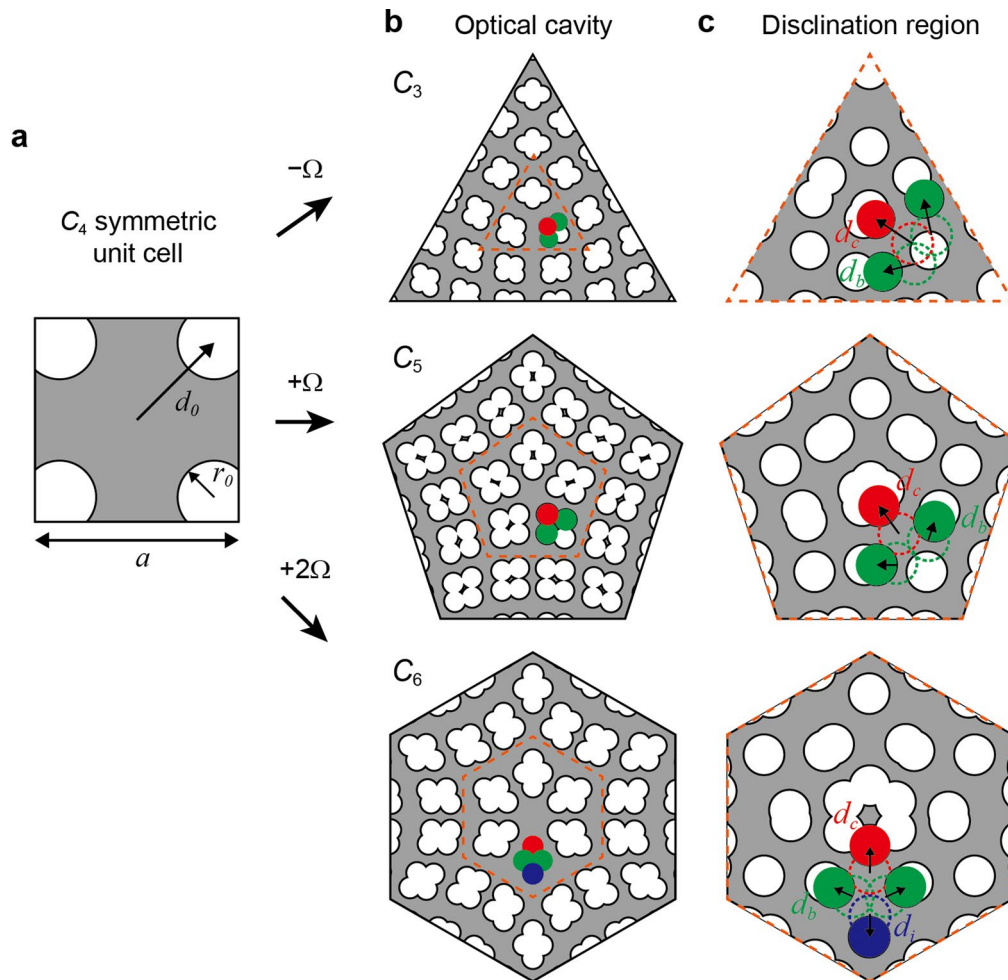
Extended Data Fig. 1 | Topological phase transition in photonic bandstructures. **a-c**, Photonic bandstructures of topologically trivial (a), symmetric (b), and nontrivial (c) unit cells. Insets, corresponding unit-cell structures. The SSH-like lattice is created with the following parameters: $a = 459$ nm, $r_0 = 0.20a$, and $h = 275$ nm, where a , r_0 , and h are the lattice constant, radius of air hole, and slab thickness, respectively. The bandstructures are calculated as a function of a center-to-hole distance, d_0 . d_0 is $0.17a$ (a), $0.35a$ (b), and $0.54a$

(c). The gray and orange regions in the bandstructures indicate the light cone and bandgap, respectively. **d**, Calculated frequency at the M point of a reciprocal lattice as a function of d_0/a . Topological phase transition occurs with varying d_0 . **e-f**, Normalized H_z field (left column) and phase profiles (right column) in the topologically trivial (e) and nontrivial (f) unit cells at the M point. The H_z field profiles for the fundamental (\blacktriangle) and second bands (\blacktriangledown) show a band inversion between the trivial and nontrivial phases.



Extended Data Fig. 2 | Detailed parameters of C_n disclination structures in TB model. The black dots represent atomic sites, and the white lines represent unit-cell boundaries. The coupling strengths of all atomic sites in the bulk lattice (gray) are the same as those in Fig. 1b, whereas the coupling strengths in the disclination region (magenta and purple) vary with atomic site positions.

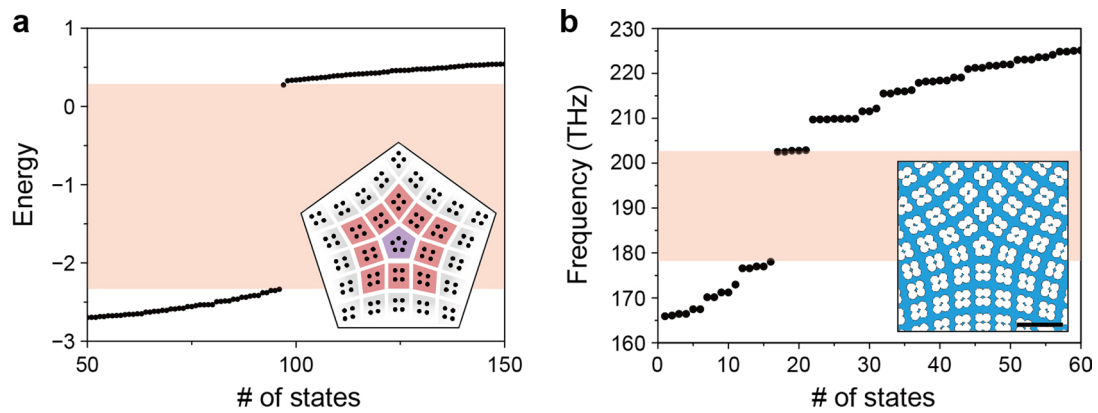
Strong coupling connects atomic sites in the disclination core (purple), whereas inverted coupling strengths to the bulk lattice define atomic sites on the disclination boundary (magenta). In our TB calculation, the weak coupling of $t_w = -0.2$ (black dashed lines) and the strong coupling of $t_s = -1.0$ (red solid lines) are set in the C_n disclination boundary.



Extended Data Fig. 3 | Photonic disclination cavities for 2D FEM simulation.

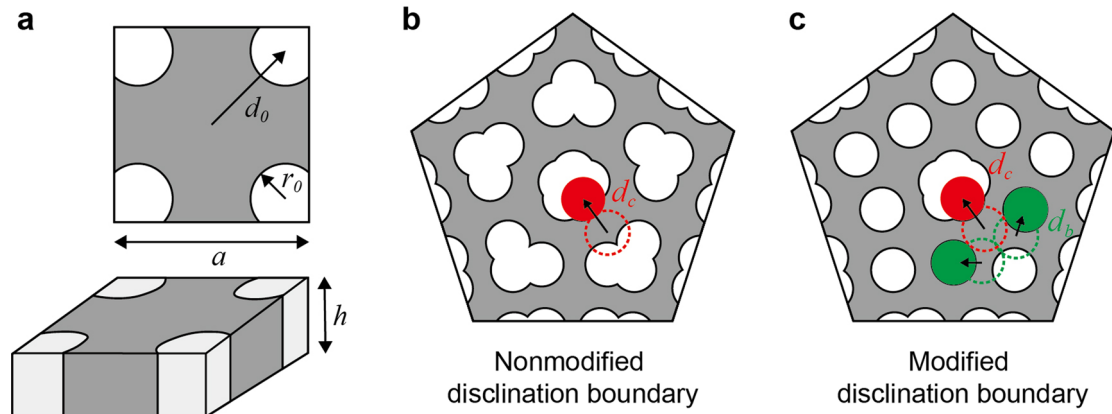
a, C_4 symmetric unit-cell structure with a lattice constant $a = 500$ nm. r_0 is the radius of air hole and d_0 is the center-to-hole distance. Three different sets of (r_0, d_0) parameters are used to convert to the C_3 , C_5 , and C_6 symmetric disclination geometries: $(r_0, d_0) = (0.25a, 0.51a)$, $(0.20a, 0.45a)$, and $(0.19a, 0.48a)$, respectively. **b**, Designed C_3 (top), C_5 (middle), and C_6 (bottom) symmetric photonic disclination cavities from the C_4 bulk lattice. These cavities are identical

to the ones in Fig. 2c,f, and i. **c**, Magnified structures inside the orange dashed regions in **b**. For each cavity, the shifting parameters of the core (d_c ; red circle), boundary (d_b ; green circle), and interior corner (d_i ; blue circle) are as follows: $(d_c, d_b, d_i) = (0.42a, 0.34a, 0)$, $(0.25a, 0.23a, 0)$, and $(0.23a, 0.20a, 0.14a)$ for C_3 , C_5 , and C_6 symmetric photonic disclination cavities, respectively. We note that the radius of the air hole at the disclination boundary is $0.14a$, and $d_c = 0.40a$, for the mode with $l=0$ in the C_6 symmetric photonic disclination cavity (Fig. 2i).

**Extended Data Fig. 4 | Topologically trivial C_3 disclination structure.**

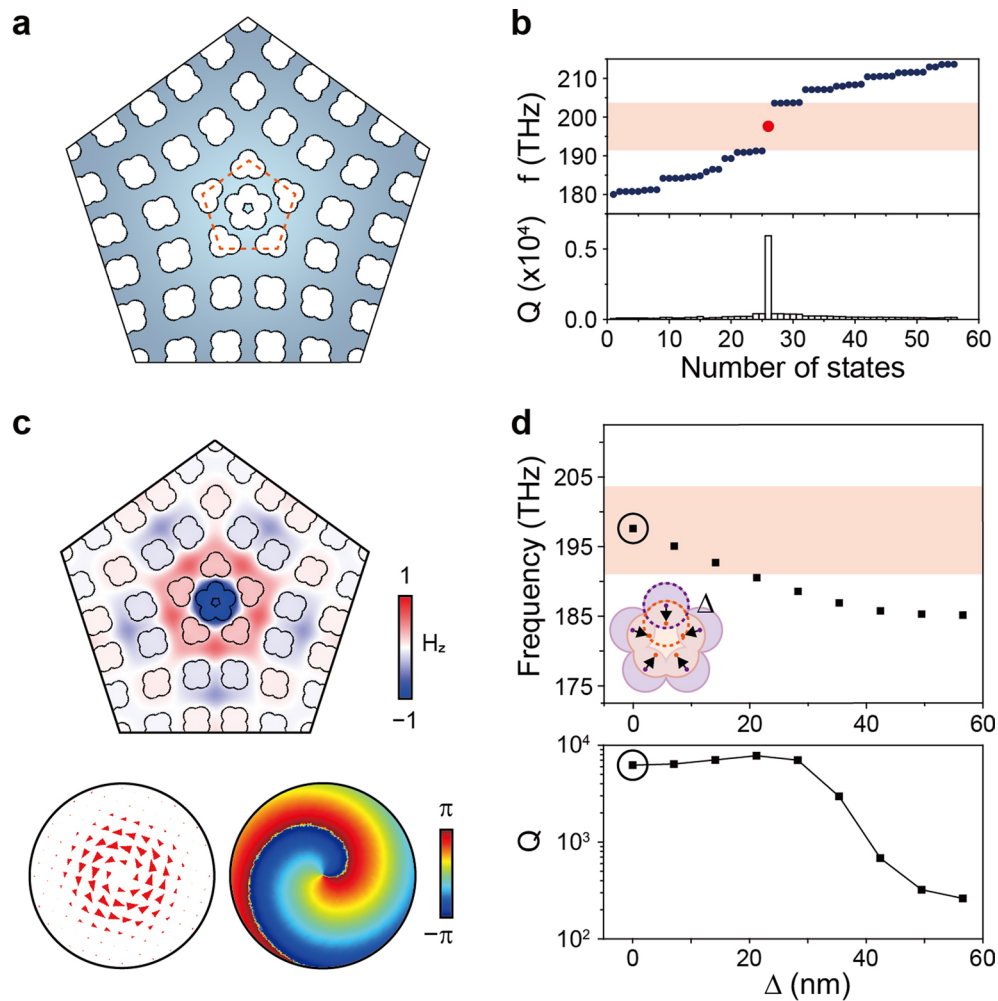
a. Calculated energy spectrum in a C_3 symmetric disclination structure based on the trivial unit cell (inset). The orange box indicates the bandgap at $t_1 = -1.0$ and $t_2 = -0.2$. Because a trivial lattice has no corner states, fractional charges are not trapped in a disclination structure³². Thus, there are no in-gap modes observed.

b. Calculated frequency of eigenmodes in a photonic disclination cavity based on the trivial unit cell (inset), which was constructed using the TB structure in **a**. Similar to **a**, no resonant mode is localized in the core of the cavity. The scale bar (inset) is 1 μm .



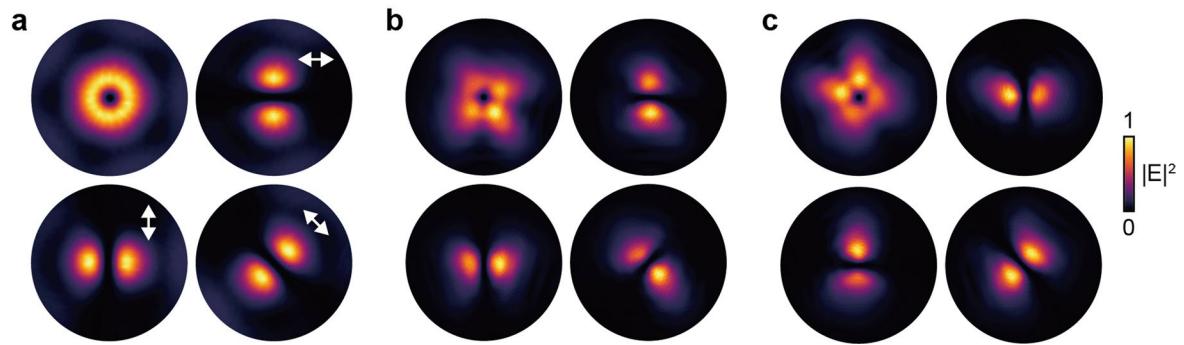
Extended Data Fig. 5 | Detailed structural parameters of 3D C_3 symmetric photonic disclination cavities. **a**, Top and tilted views of the square-lattice slab structure with the following parameters: $a = 500$ nm, $r_0 = 0.18 a$, $d_0 = 0.54 a$, and $h = 275$ nm, where a , r_0 , d_0 , and h are the lattice constant, radius of air hole, center-to-hole distance, and slab thickness, respectively. **b-c**, C_3 symmetric photonic disclination cavities with nonmodified (**b**) and modified (**c**) disclination

boundaries. The shifting parameters of the core (d_c ; red circle) and boundary (d_b ; green circle) are as follows: $(d_c, d_b) = (0.28 a, 0)$, $(0.25 a, 0.31 a)$, and $(0.40 a, 0.31 a)$ for the cavity with nonmodified disclination boundary, the expanded-core cavity with modified disclination boundary, and shrunken-core cavity with modified disclination boundary, respectively.

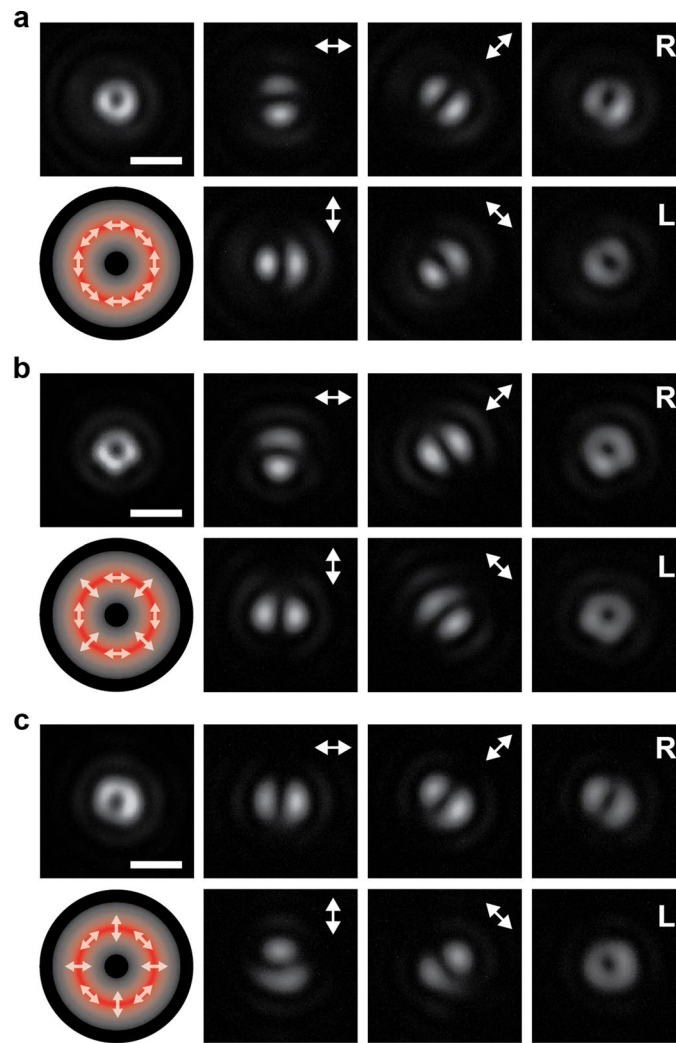


Extended Data Fig. 6 | FEM simulation in a photonic disclination cavity with a nonmodified disclination boundary. 3D FEM simulation results in the C_5 symmetric photonic disclination cavity with nonmodified disclination boundary that is designed as shown in Extended Data Fig. 5b. **a**, Photonic disclination cavity. The red dashed pentagon denotes the disclination boundary. **b**, Calculated eigenmode frequencies (top) and Q factors (bottom) for the cavity of **a**. The red dot represents the resonant mode within the photonic bandgap (orange box).

c, Optical vortex mode excited in the cavity of **a**. The H_z field (top), polarization vector field (bottom left), and phase distribution (bottom right) represent the vortex feature of $q = +1$. **d**, Calculated frequencies (top) and Q factors (bottom) of the vortex mode as a function of Δ , the center-to-center distance between air holes in the expanded and shrunken cores (inset). No other resonant mode appears in the bandgap. The black circles indicate the value of Δ for the cavity of **a**.

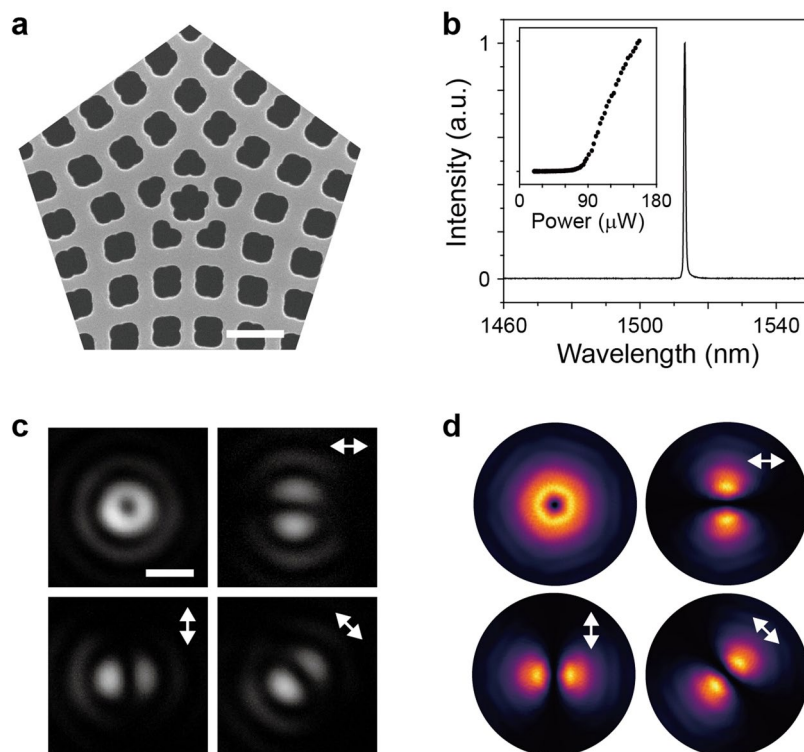


Extended Data Fig. 7 | Simulated polarization-resolved images. Far-field polarization-resolved images calculated for Fig. 3c (a), 3f (b), and 3g (c), respectively. White arrows indicate the polarization directions. The top left panel in each figure shows an unpolarized mode image. These simulated images agreed well with the measured ones in Fig. 4f-h.



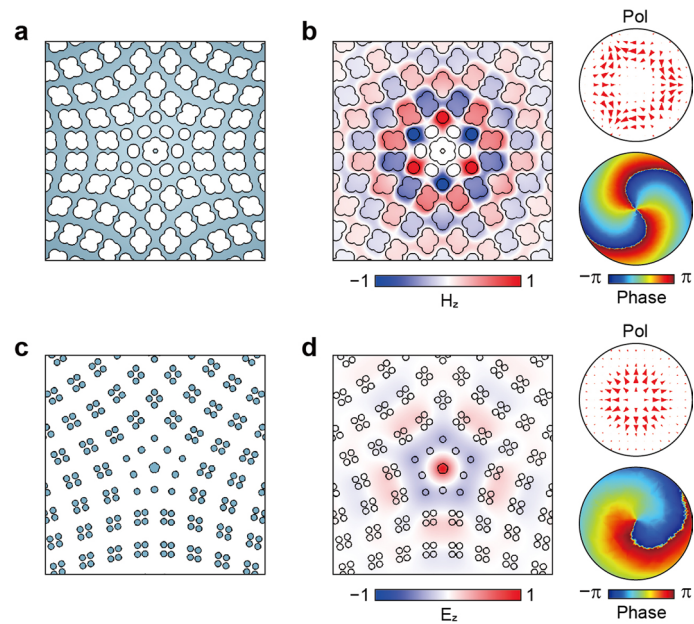
Extended Data Fig. 8 | Measured polarization-resolved images. Complete sets of measured polarization-resolved mode images from the vortex (a) and anti-vortex lasers (b and c), including 0° , $\pm 45^\circ$, 90° linearly polarized images

(middle column) and right/left circularly polarized images (right column). The images captured without a linear polarizer are shown in the top left panels. The schematics of polarization directions are shown in the bottom left panels.



Extended Data Fig. 9 | Experimental vortex nanolaser in a photonic disclination cavity with a nonmodified disclination boundary. **a**, SEM image of a fabricated C_5 symmetric photonic disclination cavity with a nonmodified disclination boundary. The scale bar is 500 nm. **b**, Measured above-threshold PL spectrum and L-L curve (inset) from the cavity of **a**. Peak wavelength and lasing threshold are 1513.2 nm and 90 μ W, respectively. **c**, Measured polarization-

resolved lasing images from the cavity of **a**. The mode profiles were captured after placing a linear polarizer in front of the IR camera. White arrows indicate the directions of the linear polarizer: 0°, 45°, 90°. The image captured without a linear polarizer is shown in the top left panel. The scale bar is 3 μ m. **d**, Simulated polarization-resolved images corresponding to **c**.



Extended Data Fig. 10 | Photonic disclination cavities for various topological charges and polarization states. Our design strategy is used to generate resonant modes with $|q| = 2$ or radial polarization. **a**, C_6 symmetric hole-type photonic disclination cavity (Fig. 2i). The colored region represents the dielectric material with a refractive index of 3.33. **b**, Optical vortex mode excited in the cavity of **a**. The H_z field (left), polarization vector field (upper right), and phase

distribution (lower right) are calculated, showing the vortex feature of $|q| = 2$. **c**, C_5 symmetric rod-type photonic disclination cavity. The colored region represents the dielectric material with a refractive index of 3.33. **d**, Radial polarization mode excited in the cavity of **c**. The E_z field (left), polarization vector field (upper right), and phase distribution (lower right) are calculated.